PROCEEDINGS OF SCIENCE

Observation of antihelium and antihypertriton in pp collisions with LHCb

Hendrik Jage[a,*] **on behalf of the LHCb collaboration**

[a] *I. Physikalisches Institut, RWTH Aachen University, Aachen, Germany*

E-mail: hendrik.jage@cern.ch

The first observation at the LHCb experiment of hypertritons and antihypertritons is reported. The used dataset consists of pp collisions at $\sqrt{s} = 13$ TeV, collected between 2016 and 2018, and corresponds to an integrated luminosity of 5.5 fb^{-1}. The hypertriton candidates are reconstructed via the two-body decay into helium-3 and a charged pion. The corresponding helium nuclei are identified with a technique that is innovative at the LHCb experiment and mainly exploits ionisation losses in the LHCb silicon sensors. A total of 1.1×10^5 prompt helium and antihelium candidates are identified with negligible background contamination and 107 ± 11 hypertriton candidates are found, paving the way for a rich programme of precise measurements of QCD and astrophysical interest to be performed on the available data.

The European Physical Society Conference on High Energy Physics (EPS-HEP2023)
21-25 August 2023
Hamburg, Germany

*Speaker

PoS(EPS-HEP2023)254

1. Introduction

One motivation to start the search for helium at LHCb was provided by the AMS-02 experiment [1] aboard the International Space Station, which has detected several potential antihelium candidates of unclear origin [2]. The observation of antihelium in Cosmic Rays could be a signature for physics beyond the Standard Model, such as dark matter annihilations, from which antihelium could be produced *e.g.* via $\overline{\Lambda}{}^0_b$ decays [3].

The LHCb detector [4, 5] is well suited to search for these $\overline{\Lambda}{}^0_b \to {}^3\overline{\mathrm{He}}\, X$ decays, as it was designed for precision measurements of rare b-hadron decays. It covers the forward pseudorapidity region ($2 < \eta < 5$), and could therefore measure helium production in a region that is unexplored by other experiments. The detector is a single-arm forward spectrometer that includes a high-precision charged-particle reconstruction (tracking) system consisting of: a silicon-strip vertex detector (VELO) that surrounds the proton-proton (pp) interaction region, a large-area silicon-strip detector (TT) located upstream of a dipole magnet with a bending power of about 4 Tm, and three stations of silicon-strip detectors (IT) and straw drift tubes (OT) placed downstream of the magnet. The tracking system measures the momentum p of charged particles with a relative uncertainty that ranges from 0.5% at low momentum to 1.0% at 200 GeV[1]. The minimum distance of a track to a primary vertex (PV), the impact parameter (IP), is measured with a resolution of $(15 + 29/p_{\mathrm{T}})$ μm where p_{T} is the component of the momentum transverse to the beam, in GeV. Different types of charged hadrons are distinguished from one another using information from two ring-imaging Cherenkov (RICH) detectors.

While being equipped to precisely reconstruct b-hadron decays, LHCb was not designed to have a helium identification capability. A new identification method [6], exploiting information from the tracking system, was therefore developed.

2. Helium identification strategy

The helium identification strategy [6] is based on the Z^2 dependence of the average energy loss per path length of a particle of charge Z passing through a silicon sensor, as modelled by the Bethe formula [7]. This information is exploited to achieve separation power between heavily-ionising helium and minimally-ionising particles of charge $Z = 1$ (bkg). It is assumed that all identified $Z = 2$ tracks are ^{3}He, due to the suppression of ^{4}He by a factor $O(10^3)$ predicted by coalescence for each additional baryon [8].

The helium identification method [6] is developed and validated on pp-collision data collected during the years 2016, 2017, and 2018, at a centre-of-mass energy $\sqrt{s} = 13$ TeV, corresponding to a total integrated luminosity of 5.5 fb^{-1}. The combined output of all LHCb physics trigger lines is used and preselected in a data reduction stage that takes place after the full reconstruction. The rigidity of each selected track, $p/|Z|$, is required to be larger than 2.5 GV and its transverse component must be at least 0.3 GV. Each track must also be of good quality and have a sufficient number of hits in the silicon detectors to enable the identification techniques discussed below.

[1]Natural units where $\hbar = c = 1$ are used throughout.

2.1 Likelihood estimators from silicon detectors

The signal induced by the energy deposition in each strip is digitised by 7-bit analogue-to-digital converters and neighbouring signal strips are typically combined into clusters of up to four strips. The counts from the strips in a cluster are added up to obtain the total cluster amplitude (ADC).

Each cluster is a separate independent measurement of a particle's energy deposit. This information is combined into a likelihood estimator. To construct this likelihood estimator, two-dimensional probability density distributions (PDD) are created for the signal and background hypotheses. One dimension of the PDD is the cluster size (CLS) and the other is the cluster ADC. The cluster distribution of singly-charged particles is thereby obtained from dedicated calibration samples of $\Lambda \to p\pi^-$ and $D^{*+} \to D^0(K^-\pi^+)\pi^+$ decays[2]. The response of the LHCb detector to ^{3}He nuclei is simulated by generating a single particle at a time at the nominal pp interaction point, and propagating it through the LHCb detector. To derive the likelihoods of the helium and background particle hypotheses, the PDDs are used as look-up tables:

$$\mathcal{L}^X = \left(\prod_{i=1}^{n} \mathrm{PDD}_i^X(\mathrm{CLS}, \mathrm{ADC}) \right)^{\frac{1}{n}}, \tag{1}$$

where $X \in \{\mathrm{He}, \mathrm{bkg}\}$, and n is the number of clusters on the track [6]. Helium and background tracks are separated using the log-likelihood ratio

$$\Lambda_{\mathrm{LD}} = \log \frac{\mathcal{L}^{\mathrm{He}}}{\mathcal{L}^{\mathrm{bkg}}} = \log \mathcal{L}^{\mathrm{He}} - \log \mathcal{L}^{\mathrm{bkg}}. \tag{2}$$

The likelihoods are evaluated separately for each sensor type and then combined for each subdetector.

3. The helium sample

The distribution of $\Lambda_{\mathrm{LD}}^{\mathrm{VELO}}$ and $\Lambda_{\mathrm{LD}}^{\mathrm{TT}}$ in the selected data is shown on the left-hand side of Fig. 1. Downstream of the magnet the tracks are required to pass $\Lambda_{\mathrm{LD}}^{\mathrm{IT}} > -1$ if they are in the IT acceptance. The remaining tracks are selected based on timing information from the OT [6].

A large, well-separated population of helium candidates is observed for $\Lambda_{\mathrm{LD}}^{\mathrm{VELO}} > 0$ and $\Lambda_{\mathrm{LD}}^{\mathrm{TT}} > -1$ (region A). Approximately 1.1×10^5 candidates are selected. Singly-charged particles are located at low values of $\Lambda_{\mathrm{LD}}^{\mathrm{VELO}}$ and $\Lambda_{\mathrm{LD}}^{\mathrm{TT}}$ (region D).

Region B is mostly populated by electrons from converted photons that are highly collinear in the VELO, but are separated by the magnetic field afterwards. Therefore, conversions are suppressed by accepting only tracks that do not share their VELO segment with another track. In addition, electron-like tracks are suppressed based on information from the RICH detectors. The remaining conversions cannot be separated by $\Lambda_{\mathrm{LD}}^{\mathrm{VELO}}$ alone, however they can be separated by $\Lambda_{\mathrm{LD}}^{\mathrm{TT}}$ and are therefore found predominantly in region B.

3.1 Estimation of residual contamination

Projections onto the $\Lambda_{\mathrm{LD}}^{\mathrm{VELO}}$ axis of the 2D distributions displayed on the left-hand side of Fig. 1 are used to estimate the level of residual background in region A. The distribution of $\Lambda_{\mathrm{LD}}^{\mathrm{VELO}}$ in

[2]The inclusion of charged-conjugate processes is implied throughout, unless stated otherwise.

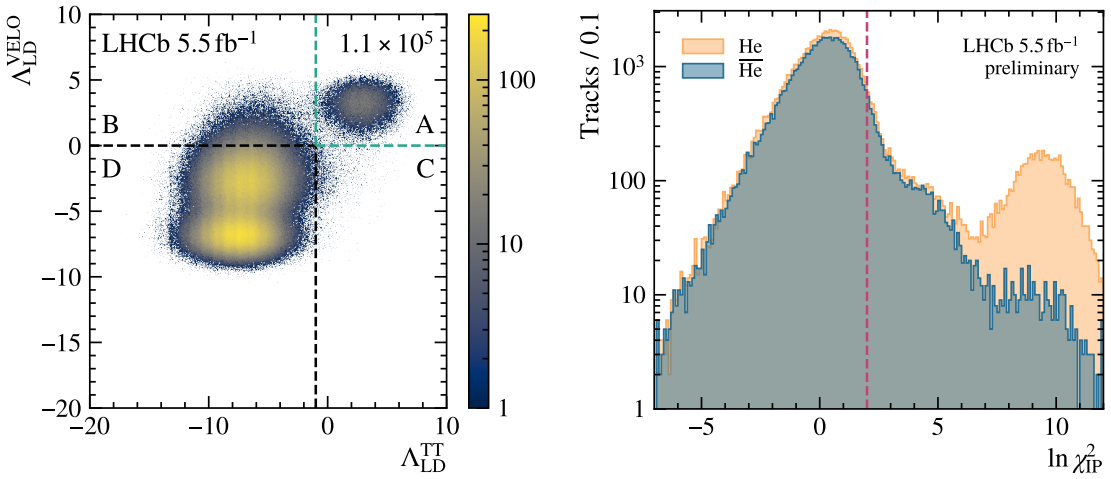

Figure 1: Left: Distributions of the log-likelihood estimators from the LHCb VELO ($\Lambda_{\mathrm{LD}}^{\mathrm{VELO}}$) and TT ($\Lambda_{\mathrm{LD}}^{\mathrm{TT}}$) silicon trackers [6]. The tracks are required to pass the downstream selection. The signal region is denoted by A, whilst regions B, C, and D correspond to background. Right: Distribution of the natural logarithm of the χ^2_{IP} for helium and antihelium tracks [9]. The requirement that separates prompt and displaced helium is shown in magenta.

background samples obtained from regions B and D ($\Lambda_{\mathrm{LD}}^{\mathrm{VELO}} < 0$) are therefore scaled to match that in region C. The remaining background level is found to be negligible and the misidentification probability for a background track to pass the helium identification is estimated to be $O(10^{-12})$ at a signal efficiency of $\sim 50\%$ [6].

3.2 Sources of helium

One variable that provides information about the origin of a helium candidate is χ^2_{IP}, which is the change of the χ^2 of the PV when it is reconstructed with or without the track. The distribution of $\ln \chi^2_{\mathrm{IP}}$ for selected helium tracks separated by charge is shown on the right-hand side of Fig. 1. So far, only prompt tracks, compatible with originating from the PV ($\ln \chi^2_{\mathrm{IP}} < 2$) have been considered. In this region, more helium (6×10^4) than antihelium (5×10^4) tracks are present.

At larger values of χ^2_{IP}, a further enhancement in the helium candidate sample, but not in the antihelium one, is observed, which is consistent with the production of helium in the detector material. The upper tail in the antihelium distribution above $\ln \chi^2_{\mathrm{IP}} > 2$ is a sign of non-prompt contributions to the sample, as expected from $\overline{\Lambda}_b^0$ or antihypertriton decays [6].

4. Hypertriton

The hypertriton ($^3_\Lambda$H) is a bound state of a proton, a neutron, and a Λ hyperon, which can be produced via coalescence in pp collisions [10, 11]. Hypernuclei provide experimental access to the hyperon-nucleon interaction through the measurement of their lifetimes and of their binding energies [12, 13]. The current estimates for the Λ binding energy and lifetime of $^3_\Lambda$H are $B_\Lambda = 148 \pm 40\,\mathrm{keV}$ and $\tau = 237^{+10}_{-9}$ ps [14]. Hyperon-nucleon interactions have significant implications for the understanding of dense astrophysical objects like neutron stars [15, 16].

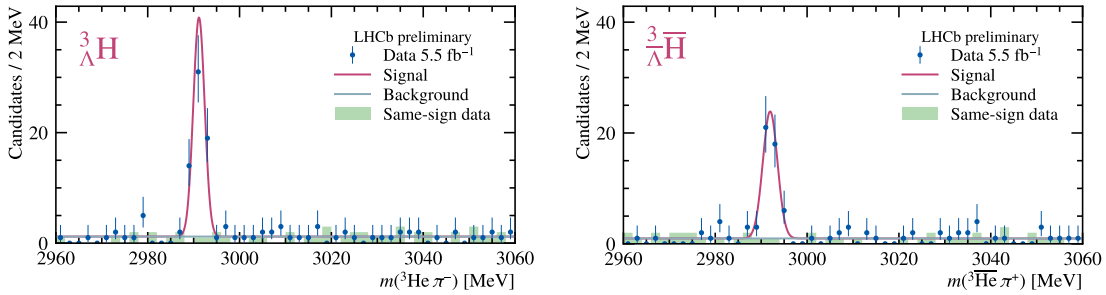

Figure 2: Invariant-mass distribution of hypertriton (left) and antihypertriton (right) candidates [9]. The models for signal (magenta) and background (green) are described in the main body. Same-sign data are shown in light green to cross-check the background level.

Hypertriton candidates are reconstructed via the two-body decay ${}^3_\Lambda\text{H} \to {}^3\text{He}\pi^-$. The lifetime of the hypertriton is large enough for it to fly a detectable distance, therefore the helium track is required to be displaced ($\ln \chi^2_{\text{IP}} > 2$). The hypertriton candidates are built from opposite-sign ^{3}He and π tracks with invariant mass $m({}^3\text{He}\pi) \in (2.96,\, 3.06)$ GeV that form a good-quality secondary vertex inside a portion of the VELO that excludes the *pp* interaction region. Furthermore, the origin of the hypertriton candidate is required to be compatible with the PV. The selection requirements are optimised to maximise the significance of the hypertriton signal [9].

The data sample is split into hypertriton and antihypertriton candidates using the charge of the helium track. The invariant-mass distributions are shown in Fig. 2 and a clear signal with a low level of background is observed in both. This observation of hypertriton serves as a validation of the developed helium identification method. An extended unbinned maximum-likelihood fit is performed on the two data sets, where the signal is modelled by a Gaussian distribution, whilst the background is modeled by a constant. The hypertriton yield $N({}^3_\Lambda\text{H}) = 61 \pm 8$ is found to be larger than the antihypertriton yield $N({}^3_{\overline{\Lambda}}\overline{\text{H}}) = 46 \pm 7$. The statistical precision on the combined hypertriton mass value is 0.16 MeV [9]. To determine the central value, charge-dependent systematic corrections still need to be investigated with simulation. They are foreseen to include effects such as energy losses in the detector, as well as hadronic interactions.

5. Summary and outlook

In these proceedings, a summary of Refs. [6, 9], covering the new helium identification method developed at LHCb, as well as its validation through the observation of hypertriton decays into ^{3}He nuclei, is given. Upcoming LHCb results will extend measurements involving helium in the so far experimentally unexplored forward region. This is expected to include measurements of the hypertriton properties and the production of helium from Λ_b^0 decays. Furthermore, the identification method is to be applied to other LHCb datasets, such as proton-ion, ion-ion, and fixed-target collision data. This is foreseen to lead to a rich programme of precise measurements of QCD and astrophysics interest.

References

[1] AMS collaboration, M. Aguilar *et al.*, *The Alpha Magnetic Spectrometer (AMS) on the international space station: Part II — Results from the first seven years*, Phys. Rept. **894** (2021) 1.

[2] S. Ting, *Latest results from AMS on the International Space Station*, 8 June 2023. https://indico.cern.ch/event/1275785/.

[3] M. W. Winkler and T. Linden, *Dark matter annihilation can produce a detectable antihelium flux through $\bar{\Lambda}_b$ decays*, Phys. Rev. Lett. **126** (2021) 101101, arXiv:2006.16251.

[4] LHCb collaboration, A. A. Alves Jr. *et al.*, *The LHCb detector at the LHC*, JINST **3** (2008) S08005.

[5] LHCb collaboration, R. Aaij *et al.*, *LHCb detector performance*, Int. J. Mod. Phys. **A30** (2015) 1530022, arXiv:1412.6352.

[6] LHCb collaboration, R. Aaij *et al.*, *Helium identification with LHCb*, arXiv:2310.05864, submitted to JINST.

[7] Particle Data Group, R. L. Workman *et al.*, *Review of particle physics*, Prog. Theor. Exp. Phys. **2022** (2022) 083C01.

[8] ALICE collaboration, S. Acharya *et al.*, *Production of deuterons, tritons, ^{3}He nuclei and their antinuclei in pp collisions at $\sqrt{s} = 0.9$, 2.76 and 7 TeV*, Phys. Rev. **C97** (2018) 024615, arXiv:1709.08522.

[9] LHCb collaboration, *Observation of antihypertriton in pp collisions with LHCb*, LHCb-CONF-2023-002, 2023.

[10] D. H. Davis, *50 years of hypernuclear physics. I. The early experiments*, Nucl. Phys. **A754** (2005) 3.

[11] P. Braun-Munzinger and B. Dönigus, *Loosely-bound objects produced in nuclear collisions at the LHC*, Nucl. Phys. **A987** (2019) 144, arXiv:1809.04681.

[12] R. H. Dalitz and G. Rajasekharan, *The spins and lifetimes of the light hypernuclei*, Phys. Lett. **1** (1962) 58.

[13] H. Kamada, J. Golak, K. Miyagawa, H. Witala, and W. Gloeckle, *Pi mesonic decay of the hypertriton*, Phys. Rev. **C57** (1998) 1595, arXiv:nucl-th/9709035.

[14] P. Eckert, P. Achenbach *et al.*, *Chart of hypernuclides — Hypernuclear structure and decay data*, 2021. hypernuclei.kph.uni-mainz.de.

[15] J. Schaffner-Bielich, in *Neutron Stars*, p. 147–208, Cambridge University Press, 2020.

[16] J. M. Lattimer and M. Prakash, *The physics of neutron stars*, Science **304** (2004) 536, arXiv:astro-ph/0405262.

PoS(EPS-HEP2023)254